Journal Name

ARTICLE TYPE

Cite this: DOI: 10.1039/xxxxxxxxxx

Received Date
Accepted Date

DOI: 10.1039/xxxxxxxxxx

www.rsc.org/journalname

Dissolution of anionic surfactant mesophases

Andreas S. Poulos,*[a] Christopher S. Jones,[b] and João T. Cabral *[a]

Linear and circular solvent penetration experiments are used to study the dissolution of anionic SLE_3S surfactant mesophases in water. We show that a lamellar (L_α) phase in contact with water will transit through a series of cubic, hexagonal, and micellar phase bands with sharp interfaces identified from their optical textures. In both linear and circular geometries, the kinetics of front propagation and eventual dissolution are well described by diffusive penetration of water, and a simple model applies to both geometries, with a different effective diffusion coefficient for water D_f as the only fitting parameter. Finally, we show a surprising variation of dissolution rates with initial surfactant concentration that can be well explained by assuming that the driving force for solvent penetration is the osmotic pressure difference between neat water and the aqueous fraction of the mesophase that is highly concentrated in surfactant counterions.

1 Introduction

Surfactants are present in numerous formulated products such as detergents, shampoos, fabric softener, paints, pharmaceuticals, and foods[1]. At elevated concentrations, surfactant solutions self-assemble into lyotropic mesophases[2], exhibiting complex rheology and viscoelasticity relevant to processing[3,4]. The equilibrium phase behavior of surfactant solutions has been extensively studied for different amphiphilic molecules and solvents[5,6]. Non-equilibrium processes, on the other hand, are less well understood and remain a subject of fundamental and industrial interest[7].

In particular, understanding the dissolution of concentrated surfactant solutions in different solvents is critically important for their effective industrial processing, as end-product concentrations are generally much lower than feed concentrations ($c \geq 70\%$). A typical dissolution pathway will lead to the sequential formation of different mesophases that depending on their specific microstructure might have significantly varying physical (optical, detergency, etc) and rheological properties.

Surfactant dissolution has mainly been studied using solvent penetration experiments[8–11] and by simulations[12–14]. In a solvent penetration experiment, a concentrated surfactant solution is brought into contact with its solvent. Provided that myelinic instabilities do not form[15,16], interdiffusion creates a continuous concentration gradient perpendicular to the interface and hence the succession of phases upon dilution can be determined by appropriate analytical techniques such as polarized light optical microscopy, small-angle X-ray scattering, and IR spectroscopy.

Solvent penetration experiments have traditionally been used to establish approximate phase diagrams in a variety of systems[10,17–23]. It is well established that in such an experiment phase transformation happens on much faster timescales than interdiffusion[9,24]. Hence, the local surfactant concentration determines the mesophase directly, according to the equilibrium phase diagram of the system. Recently, a similar method has also been proposed where evaporation through PDMS is used to produce appropriate concentration gradients in a microfluidic device[25–27].

Dissolution is of course an important process for a variety of other systems such as solid granules and polymeric particles, especially in the context of drug delivery[28–31] and even gas bubbles[32–34]. As such, a plethora of experimental methods and theoretical approaches have been used to understand and describe the process. However, surfactant dissolution is subtly different in that a significant amount of solvent may penetrate into the initial phase, which can be much faster than the diffusion-controlled advection of surfactant molecules at the dissolution boundary. In that respect, it has more in common with the dissolution of glassy polymers that are considerably swelled by the solvent before dissolving[35].

In this paper, we use simple millifluidic devices to perform linear and circular solvent penetration experiments of lamellar and hexagonal phases of the anionic sodium lauryl ether sulphate (SLE_3S) surfactant in contact with water. The paper is structured as follows. Firstly, we determine the kinetics of water penetration and surfactant dissolution in linear microchannel experiments and show that they can be described by a simple effective diffusion model with one adjustable parameter. Then we establish the kinetics of dissolution of cylindrical surfactant drops and show that the same model applies. Finally, we measure the dis-

[a] Department of Chemical Engineering, Imperial College London, London SW7 2AZ, United Kingdom. E-mail: a.poulos@imperial.ac.uk, j.cabral@imperial.ac.uk
[b] Procter & Gamble, Brussels Innovation Centre, Temselaan 100, B-1853 Strombeek-bever, Belgium.

solution of mesophases with different initial surfactant concentrations. We determine the dissolution pathways and propose a general framework to rationalise the sequential phase change and associated kinetics.

2 Materials & Methods

2.1 Surfactant & Solvents

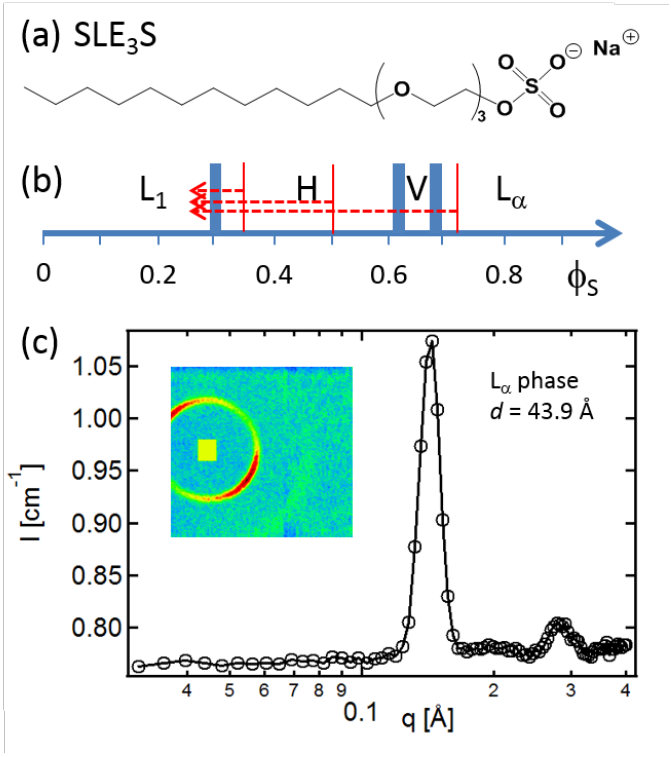

Fig. 1 (a) Chemical structure of sodium lauryl ether sulphate (SLE_3S) surfactant. (b) Approximate phase diagram of the SLE_3S surfactant. When dissolving, the initially lamellar (L_α) phase transforms into a cubic phase (V), a hexagonal phase (H), and finally an isotropic micellar phase (L_1). This and other dissolution pathways starting from the hexagonal (H) phase are shown with red arrows. (c) Small-angle neutron scattering pattern of the initial SLE_3S/water phase with $\phi(SLE_3S)$=0.72 confirms lamellar phase with repeat distance d = 43.9 Å. Inset: 2D SANS pattern under partial alignment of the lamellar phase.

Sodium lauryl ether sulphate (SLE_3S) surfactant solution (ref. STEOL-CS-370) was obtained from Stepan (IL, USA) and used as received. The paste contains 72% volume fraction surfactant in water. The chemical structure of the SLE_3S surfactant is shown in figure 1a. The hydrophilic head comprises three ether groups and a charged SO_3^- group at the end with a sodium counterion, and its structure is similar to the ubiquitous sodium dodecyl sulphate (SDS) surfactant except for the three extra ether groups. Since we are not aware of a published phase diagram for SLE_3S, an approximate diagram based on polarized light optical microscopy textures and macroscopic sample observations was obtained and is shown in figure 1b. The initial paste at $\phi_s = 0.72$ is in the fluid lamellar (L_α) phase, as confirmed by small-angle neutron scattering which also allows the determination of the repeat distance $d = 43.9$Å from the first peak position as $d = \frac{2\pi}{q_{001}}$ (Figure 1c). The lamellar phase persists down to $\phi_s \approx 0.67$. As the concentration decreases further, the lamellar phase gives way to an isotropic cubic phase ($\phi_s \approx 0.62 - 0.68$), and then to a hexagonal phase ($\phi_s \approx 0.30 - 0.62$). Below $\phi_s^* \approx 0.30$, the samples become isotropic indicating a micellar phase. The dissolution pathway from the initial lamellar phase to the isotropic micellar phase is shown in figure 1b with an arrow. Millipore water is used for the dissolution experiments.

2.2 Microfluidic device preparation

Devices were fabricated by single step frontal photopolymerization (FPP) of a thiol-ene copolymer (NOA 81, Norland Adhesives) within standard microscope slides of 75 by 25 mm size following previously published procedures[36–39]. In short, the microchannel was formed by selective UV-A exposure with a photomask, and the unexposed monomer was removed from the channel by repeated flushing with ethanol and acetone. A hole was drilled with a diamond tip drill bit on the top slide, and a nanoport (N-333 NanoPort, 10-32 Coned, IDEX Health & Science) was attached to the top of the device with cyanoacrylate super glue. The nanoport allows quick connection of tubing and was used as the inlet for the microfluidic channel.

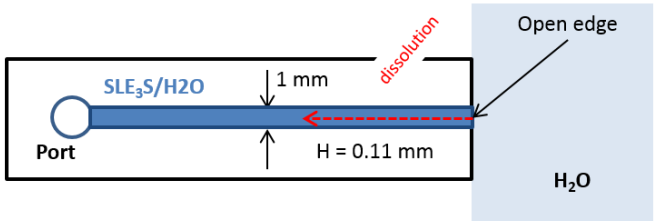

Fig. 2 Schematic of the device used in linear penetration experiments (not to scale). The channel is sandwiched between two glass slides and has a 1 mm width and a 0.11 mm height. The channel is filled with SLE_3S/water through a port drilled on the top glass slide. The other end of the channel is open and allows the H_2O to come into contact with the surfactant solution.

2.3 Linear and circular penetration experiments

A schematic of the device used in the linear penetration experiements is shown in 2. A straight channel of 1 mm width was formed between the inlet and the open edge of the device. The channel is filled with surfactant paste using a syringe connected to the inlet. The whole device is placed in a glass container under a microscope objective. The container is then filled with the solvent up to the height of the top slide. Thus the open edge of the channel comes into contact with the solvent which marks the start of the linear dissolution experiment. The device is reusable by flushing with water and then air. For the circular penetration experiments, a drop of surfactant paste is deposited between two glass slides separated by a 0.11 mm spacer. The two slides are clamped together and water is allowed to penetrate between them by capillarity eventually coming into contact with the surfactant drop.

2.4 Small Angle Neutron Scattering

The SANS experiments were carried out at the D22 diffractometer, Institute Laue Langevin (Grenoble, France), with an incident neutron wavelength of $\lambda = 6$ Å, collimation of 5.6 m, and two sample-detector distances of 1.4 m and 5.6 m.

2.5 Optical microscopy

Optical birefringence texture images were obtained with an Adimec A-1000 CCD camera at 20-25 s intervals mounted on an BX40 Olympus transmission microscope with a 5x Olympus objective lens. The experiment usually lasted 1-2 hours resulting in a series of 200-300 images. Analysis was performed with ImageJ and the dissolution front identified by the large intensity difference of the birefringent hexagonal phase and the non-birefringent micellar phase. The intensity profiles along the long axis of the channel were generated by the ImageJ macro 'StackProfilePlot'. The front position was then tracked by a custom macro written for Igor Pro 6 and calibrated to distance^2 vs time plots. The tracking of the subsidiary fronts was done manually as the intensity difference is comparatively smaller. A similar procedure was employed for circular front tracking.

3 Results & Discussion

3.1 Shear alignment of lamellar phase

The SLE_3S paste was inserted inside the channel by injection with a syringe. In figure 3 we show that channel shear flow along the channel aligns the lamellar phase to a great extent, which can be seen by polarized microscopy. When the channel axis is at 45° with respect to the crossed polars, maximum birefringent intensity is observed (Figure 3a); when the long axis is parallel to the analyser, no birefringence is detected and the sample appears dark except at the curved interfaces around the bubbles (Figure 3b). As the lamellar phase is uniaxial, the director thus points perpendicularly to flow with all the bilayers aligned in a monodomain parallel to the flow direction. In figure 3c the texture of the aligned phase is shown in more detail. It has all the characteristics of a lamellar phase aligned in planar orientation such as oily streaks with striations parallel to the flow direction[40].

3.2 Dissolution

Linear penetration experiments were performed to study the kinetics of dissolution of this highly aligned L_α phase. After injection, excess surfactant was carefully removed from the open end of the channel so that the initial interface was flat (Figure 4a). The lamellar phase was then quickly brought into contact with water. Already after 300 s, the initially uniform lamellar phase has developed a series of sharp bands perpendicular to the long axis of the channel (Figure 4b). The interfaces separating adjacent bands are flat indicating that, in this geometry, the dissolution process is taking place in one dimension. Each of these bands has its own characteristic birefringent texture and corresponds to a specific phase in the dilution path of the SLE_3S. Hence, the first narrow band that appears after the lamellar phase corresponds to the narrow cubic domain in the phase diagram of figure 1b. Although the cubic phase is isotropic, here it appears weakly birefringent with a characteristic texture similar to that of the preceding lamellar phase. This is most likely due to a trace amount of lamellar phase still present close to the walls of the channel where the thermodynamics and kinetics of phase transformation are altered by the presence of a solid-liquid interface. The presence of a solid surface has been previously found to induce partial short-range order and produce a surface memory effect[41,42]. The next band corresponds to the hexagonal phase at intermediate surfactant concentrations. In contrast to the initial lamellar phase, the hexagonal phase is not oriented in a monodomain with some particular orientation with respect to the long axis of the capillary. This is expected as it develops from the isotropic cubic phase which has erased memory of the initial macroscopic monodomain bilayer orientation.

Similarly, the first interface that moves most rapidly and is furthest away form the open end of the channel corresponds to the transition from the lamellar phase (L_α) to the cubic phase (V). The second interface corresponds to the cubic (V) to hexagonal (H) phase transition. The third interface corresponds to the hexagonal (H) to micellar (L_1) phase transition. After 1500 s the position of the sharp interfaces has moved even further away from the open end of the capillary (Figure 4c). At the same time, the width of the cubic, hexagonal, and micellar bands has also increased. Finally, after 3900 s two of the interfaces and the cubic band have moved off the field of view of the microscope and only the hexagonal and micellar bands are visible (Figure 4d). This succession of phases is also shown in the bottom panel of Figure 4 as a schematic, with a red arrow indicating the progression of the dissolution front (the interface between the hexagonal and the micellar phase).

3.3 Diffusive propagation of fronts

Based on these series of images the position of each interface can be tracked as the dissolution proceeds. In figure 5a, we show that the position squared (L^2) of the interface with respect to the open end of the channel is found to be a linear function of time for all interfaces. This scalling establishes the diffusive nature of the process. Effective diffusion coefficients, D_{eff}, for all fronts can be calculated from the data in figure 5. The fastest interface (L_α to cubic) has $D_{\text{eff}} = 27.5\,10^{-10}\,\text{m}^2/\text{s}$; this is reduced to $19.1\,10^{-10}\,\text{m}^2/\text{s}$ for the cubic to hexagonal interface, and $3.3\,10^{-10}\,\text{m}^2/\text{s}$ for the hexagonal to micellar interface which sets the overall timescale for the dissolution process, as the rate-limiting step. A consequence of the diffusive propagation of all fronts is that the widths of the cubic and hexagonal bands in figure 4 also grow diffusively with time with an effective diffusion coefficient given by the D_{eff} of the two bounding interfaces:

$$w^2 = (\sqrt{D_{\text{eff},1}t} - \sqrt{D_{\text{eff},1}t})^2 = \left(D_{\text{eff},1} + D_{\text{eff},2} - 2\sqrt{D_{\text{eff},1}D_{\text{eff},2}}\right)t$$

From the succession of images in figure 4, it is clear that a significant amount of solvent penetrates into the liquid crystalline phase. Locally this reduces the surfactant concentration and drives the phase change quasi-instantaneously as it has been previously reported[8,11]. Hence, in contrast to dissolution of solids which is mainly controlled by transport of material away from

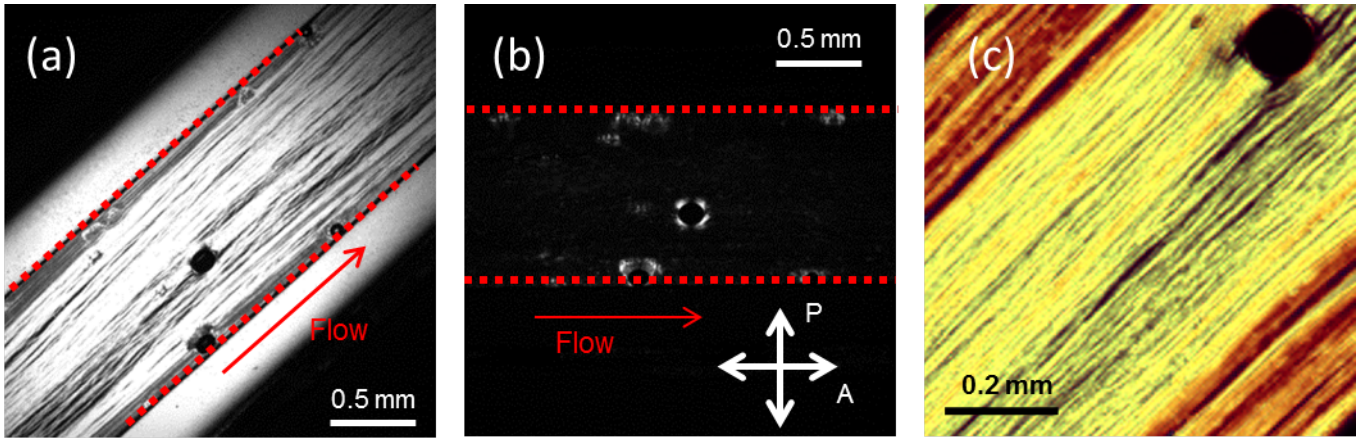

Fig. 3 Demonstration of lamellar phase shear alignment: Polarized light optical microscopy images of SLE_3S paste inside the channel. The polarizer and analyser are aligned vertically and horizontally respectively. (a) Capillary axis is rotated to 45^o with respect to the polarizer/analyser the birefringent intensity is maximized. (b) Capillary axis parallel to analyser: total extinction of birefringence except in the vicinity of bubbles. (c) Texture of the SLE_3S paste showing a planar alignment of the lamellar phase.

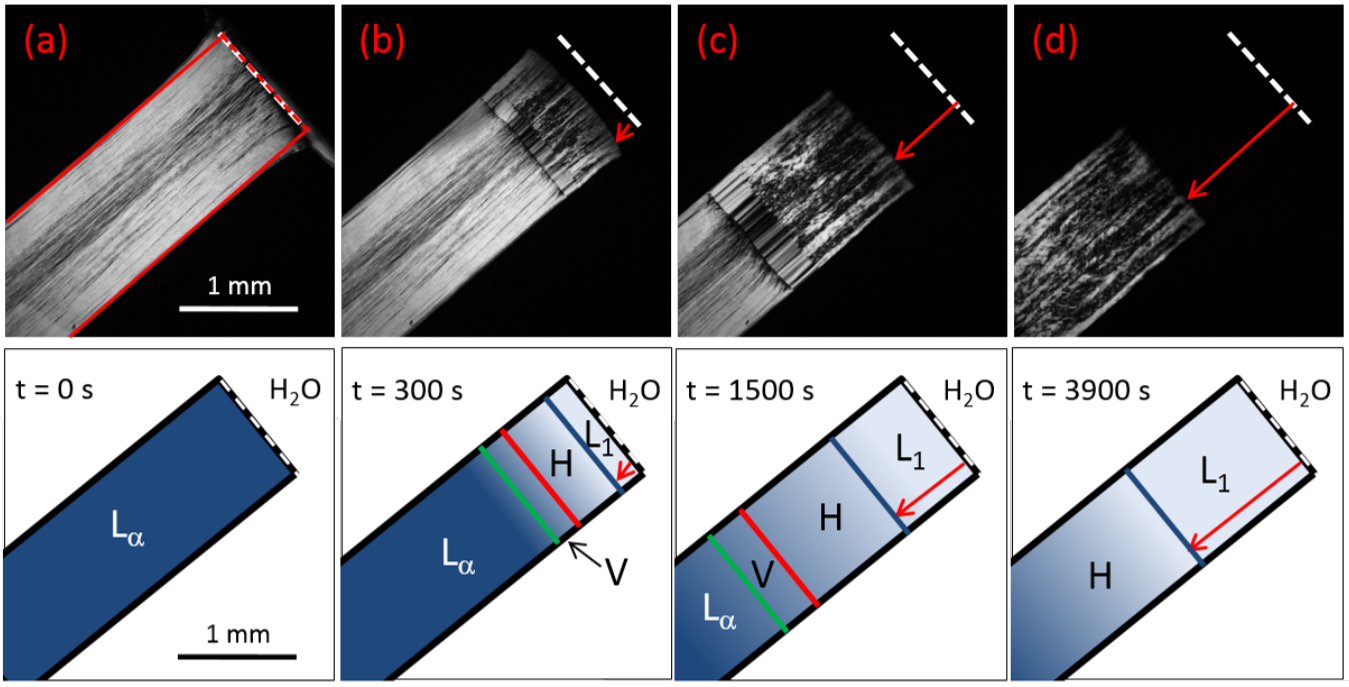

Fig. 4 Polarized light optical microscopy images of dissolving lamellar phase inside microchannel. The open end of the channel is shown with a white dashed line. (a) Before contact with solvent (b) t = 300 s after contact with solvent (c) t = 1500 s, (d) t = 3900 s. The open edge of the channel is marked with a white dashed line. (Bottom panel) Schematic showing the development of the different bands that correspond to the lamellar (L_α), cubic (V), hexagonal (H), and micellar isotropic (L_1) phases. The red arrow corresponds to the progression of the dissolution front.

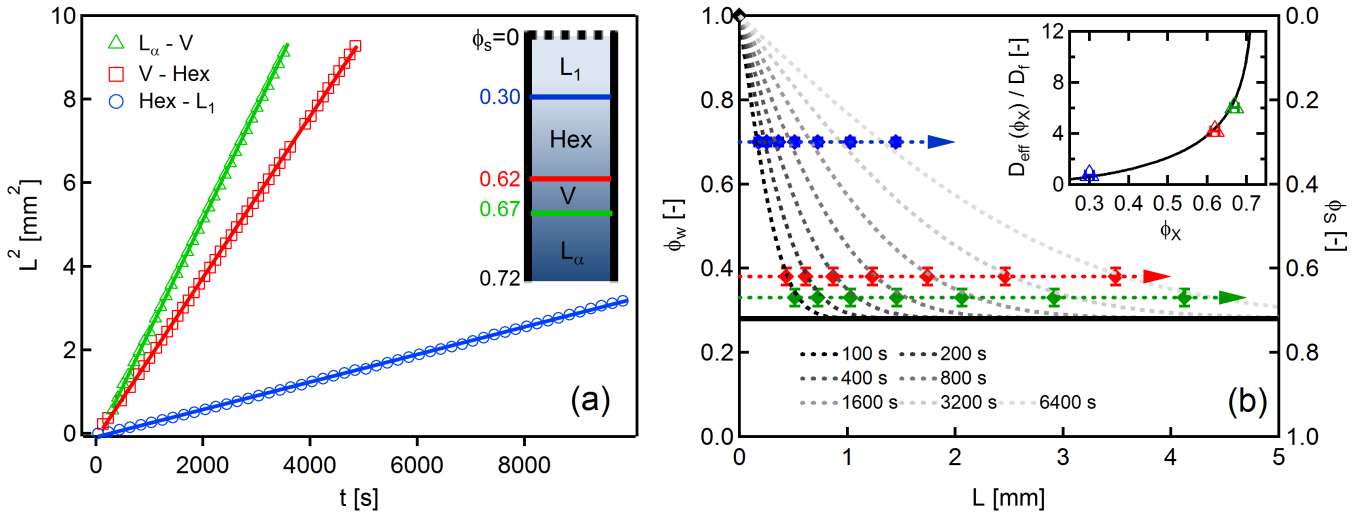

Fig. 5 (a) Square of propagation distance from the open edge of the three fronts against time. The blue triangles correspond to the lamellar (L_α) to cubic (V) front, the red squares to the cubic (V) to hexagonal (Hex) front, and the green circles to the hexagonal (Hex) to micellar (L_1) front, as illustrated in the inset schematic. The lines are linear fits to the three sets of data to extract effective diffusion coefficients. (b) Concentration profiles along the channel for different times after the initial contact of water with the surfactant. The data points indicate the positions of the three fronts as the dissolution proceeds. The dashed lines are fits of equation 1 as described in the text. Inset: Effective diffusion coefficients for the lamellar-to-cubic (green), cubic-to-hexagonal (red), and hexagonal-to-micellar (blue) fronts, normalized by the model fitting parameter D_f. The continuous line shows the predicted variation of D_{eff} with surfactant volume fraction given by equation 2 based on the model discussed in the text.

the solid-liquid interface, here dissolution is also affected by penetration of solvent into the liquid crystalline phase. The difference in physical mechanism means that the classical models used for predicting kinetics of dissolving solid or gas particles[28,32] are not strictly applicable, as these solve the diffusion equation *outside* the dissolving substance.

Since the phase transformation is locally very fast, the fronts track fixed values of the surfactant volume fraction ϕ_S (or equivalently water $\phi_w = 1 - \phi_s$) given by the equilibrium phase diagram of the surfactant (figure 1b). Hence the front kinetics data of figure 5a can be re-plotted in a concentration-distance graph yielding the time evolution of the concentration profile inside the channel. This is shown in figure 5b where the data points correspond to the time evolution of the front positions. Evidently, the time evolution of the concentration profile can only be known with certainty at the three transition concentrations, $\phi_s = 0.30, 0.62, 0.67$ ($\phi_w = 0.70, 0.38, 0.33$) for the dissolution, cubic-to-hexagonal, and lamellar-to-cubic fronts respectively.

The simplest model that can be used to obtain the full concentration profile and its time evolution makes the strong assumption that the dominant mechanism in the dissolution process is diffusive water penetration from the open edge of the channel. Given that the channel is much longer than the penetration depth, we can write down the solution to the diffusion equation in a semi-infinite 1D medium[43]:

$$\frac{\phi_w(L,t) - \phi_{w,1}}{\phi_{w,0} - \phi_{w,1}} = \text{erf}\left(\frac{L}{2\sqrt{D_f t}}\right) \qquad (1)$$

where $\phi_w(L,t)$ is the water volume fraction with boundary values $\phi_{w,0} = 0.28$ at $x = +\infty$ (open end) and $\phi_{w,1} = 1$ at $x = 0$. In figure 5b, the dashed lines show least-square fits of equation 1 with D_f as a fitting parameter on the front kinetics data points. It is clear that even this simple model can fit the data with a high degree of accuracy. Significantly, the fitting parameter D_f extracted from the fits is virtually identical for all seven curves that represent different times from 100s to 6400 s. Hence, equation 1 with $D_f = 4.55\,10^{-10}\,\text{m}^2/\text{s}$ yields, to a very good approximation, the spatio-temporal evolution of the concentration profile in linear penetration experiments of the SLE_3S surfactant.

This model although relatively simple has some interesting features. It predicts the diffusive kinetics of any surfactant concentration ϕ_X:

$$L^2(\phi_X) = 4D_f \left[\text{erf}^{-1}\left(\frac{\phi_X}{\phi_s^{\text{init}}}\right)\right]^2 t \qquad (2)$$

where $\phi_s^{\text{init}} = 1 - \phi_{w,0} = 0.72$ is the initial surfactant concentration. The concentration dependent effective diffusion coefficient is shown in the inset of figure 5b (continuous line), normalized by D_f. The actual values for the three fronts are plotted on the same graph and, of course, show good agreement with the model prediction. It is clear that, in the context of this model, the D_{eff} diverges at the initial $\phi_X = 0.72$ and approaches zero as $\phi_X \to 0$. Hence the different front speeds emerge as a natural consequence of water diffusion into the surfactant phase.

It is perhaps surprising that such a simple model can satisfactorily capture the main features of the complex dissolution process. The two main drawbacks are that it does not take into account the potentially different diffusion coefficients of the phases along the dissolution pathway[8,12] and also it does not take into account

the accompanying swelling of the surfactant phases upon ingress of water. However, both these effects are diffusive and hence they are incorporated in an effective D_f. This in turn restricts the interpretation of D_f in terms of more fundamental quantities (e.g. water self-diffusion).

3.4 Concentration dependence

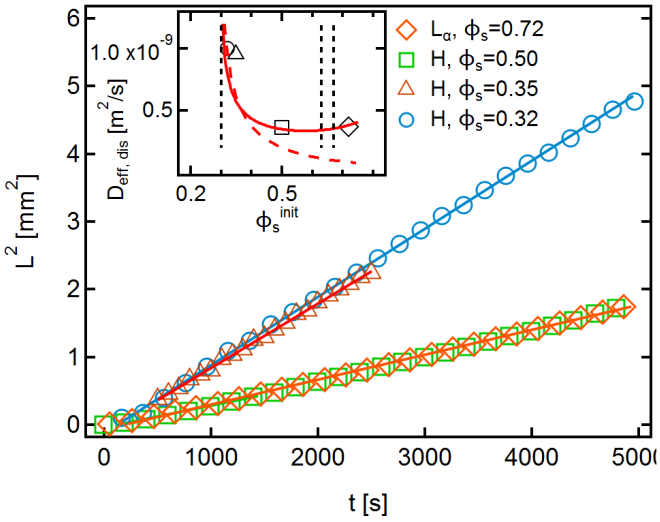

Fig. 6 Dissolution front kinetics for different initial surfactant volume fractions ϕ_s^{init}. Inset: Effective diffusion coefficient of the dissolution front as a function of initial surfactant volume fraction. The red dashed line is a prediction based only on equation 2, and the solid red line a prediction of the extended model that includes an osmotic pressure contribution given by equation 3. The vertical lines indicate the positions of the phase boundaries.

Figure 6 shows the propagation kinetics of the dissolution front for different initial surfactant concentrations ϕ_s^{init}. These results are only shown for the dissolution front because in the case of lower initial surfactant concentrations the material is already in the hexagonal phase and hence only the hexagonal to micellar interface appears in the dissolution path. It is clear that in all cases the front propagation is also diffusive in character. However, the variation of the effective diffusion coefficient with surfactant concentration is highly non-linear. This is quite evident by comparing the dissolution kinetics of the hexagonal phase at $\phi_s^{\text{init}} = 0.5$ with that of the original lamellar phase at $\phi_s^{\text{init}} = 0.72$ (squares vs diamonds in figure 6). The two are indistinguishable leading to the same effective diffusion coefficient as seen in the inset of figure 6. This result is quite surprising as one could intuitively expect that the lower concentration phase, which is closer to the phase boundary, dissolves faster. However, only surfactant concentrations much closer to the micellar phase boundary (e.g. $\phi_s^{\text{init}} = 0.32$ shown with triangles in figure 6) exhibit significantly faster dissolution with an effective diffusion coefficient 2.5 times larger.

This highly non-linear variation of the effective diffusion coefficient can be partly understood by referring back to the water penetration model. Equation 2 can predict effective diffusion coefficients for the dissolution front ($\phi_X = 0.30$) as a function of ϕ_s^{init}. The model prediction though does not agree well with the experimental data (red dashed line in the inset of figure 6). The prediction can be improved by considering the driving force for water penetration into the surfactant phase. For a charged surfactant like SLE_3S, the Na^+ counterion concentration inside the aqueous part of any mesophase will be relatively high. Hence, there will be a high osmotic pressure gradient perpendicular to the interface that will act as a driving force for the penetration of neat water into the surfactant phase [16,44]. We can estimate the osmotic pressure by assuming that we have a gas of counterions that are free to move only inside the aqueous part of the mesophase. Hence, the Na^+ counterion concentration is directly proportional to the surfactant volume fraction (ϕ_s^{init}) but also inversely proportional to the water volume fraction as they are excluded from the hydrophobic part of the mesophase. For a more complete calculation of the osmotic pressure, the Poisson-Boltzmann approximation can be used [45] but this is not necessary in the context of this work. Taking all that into account we have to add a factor of $\phi_s^{\text{init}}/(1-\phi_s^{\text{init}})$ to the prediction of equation 2. Hence,

$$D_{\text{eff, dis}}\left(\phi_s^{\text{init}}\right) = 4D_f\left[\text{erf}^{-1}\left(\frac{\phi_X}{\phi_s^{\text{init}}}\right)\right]^2 \frac{\phi_s^{\text{init}}}{1-\phi_s^{\text{init}}} \qquad (3)$$

The predicted variation is shown with a solid red line in the inset of figure 6 and agrees rather well with our results. It predicts that D_{eff} is essentially independent of the initial surfactant concentration in a wide range of ϕ_s^{init} between 0.45-0.72.

3.5 Dissolution of cylindrical drops

Qualitatively the same observations can be made on a dissolving cylindrical drop of SLE_3S surfactant at 0.72 of initial radius R_0. Experimentally, this is realized by sandwiching a droplet between two glass microscope slides with a 0.11 mm spacer. At $t = 0$, the drop comes into contact with water (figure 7a). After 100 s a series of circular interfaces have appeared within the drop. The initial lamellar phase is in the middle of the drop, surrounded by a thin cubic shell and the hexagonal shell on the outside of the drop (figure 7b). As the interfaces continuously progress towards the center of the droplet, the widths of the cubic and hexagonal shells increase (figure 7c). After 1600 s, the initial lamellar phase has been completely transformed into a hexagonal phase that in turn has dissolved into a micellar phase decreasing the radius of the drop (figure 7d). This particular drop completely dissolves after 2250 s.

The kinetics of water penetration and dissolution are shown in figure 8. As expected and in contrast to the linear penetration experiments, the kinetics in circular geometry depend on the initial size of the drop. This can clearly be seen in figure 8a where the blue points indicate the radius squared (R^2) of five drops with different initial radii R_0 in the range $0.7 - 1.1$ mm plotted against time after water contact. All the curves have a similar shape but the initially smaller drops dissolve faster than the larger drops. The same is true for the radius of the cubic-to-hexagonal interface shown here for three of the drops (red points in figure 8a). The effect of the circular geometry can be taken into account by renor-

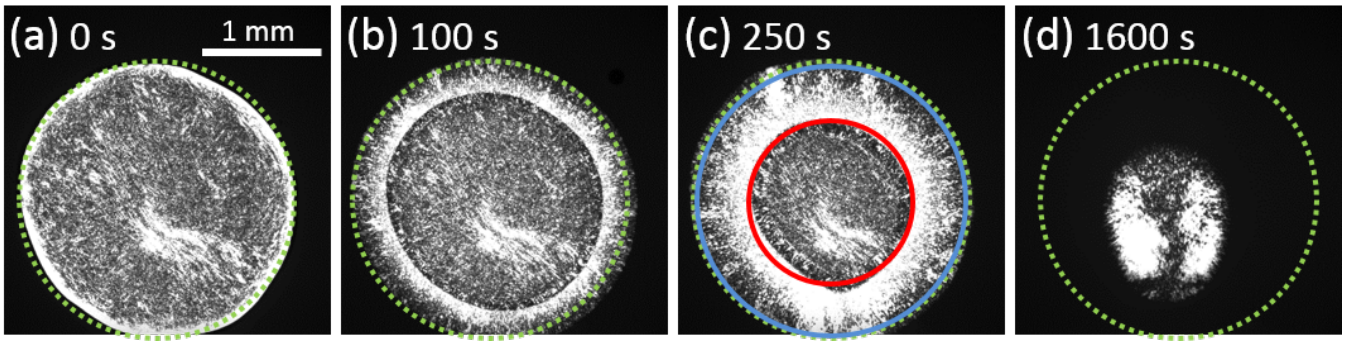

Fig. 7 Circular penetration experiments. A cylindrical drop of surfactant ($\phi_s = 0.72$) of radius $R_0 = 1.15\,\mathrm{mm}$ is sandwiched between two microscope slides with a 0.11 mm spacer. At t=0 the drop comes into contact with water and the dissolution process begins. Similarly to the linear penetration experiments, a series of circular interfaces appears within 100 s. The interfaces move towards the center of the drop demarcating the lamellar, cubic, hexagonal, and micellar phases. After 1600 s only the hexagonal phase remains and the drop has dissolved and shrunk to a fraction of its original size shown by the green dashed circle in all subfigures. The position of the two fronts that we track are shown in (c): cubic-to-hexagonal (red) and hexagonal-to-micellar (blue).

malizing both axes by the initial radius squared R_0^2. In figure 8b, we show that using this renormalization, we can obtain master curves for the kinetics of the dissolution and cubic-to-hexagonal fronts that are independent of the initial radius of the drop.

We have seen before that the water penetration and dissolution kinetics in linear penetration experiments can be modeled accurately by considering only the diffusion of water into the surfactant phase. A similar model can be built to describe the results of the circular penetration experiments. The initial conditions are that $\phi_w(r < R_0) = 0.28$ and $\phi_w(r > R_0) = 1$, and the boundary condition is that far from the drop the surface, at $r = a$, is maintained at a constant water volume fraction $\phi_w(r = a, t) = 1$. Following Crank[43], we can write down the solution of the diffusion equation in cylindrical coordinates as:

$$\phi_w(r,t) = \phi_0 \left\{ 1 - \frac{2}{a} \sum_{n=1}^{\infty} \frac{1}{\alpha_n} \frac{J_0(r\alpha_n)}{J_1(a\alpha_n)} \exp\left(-D_f \alpha_n^2 t\right) \right\} + \frac{2}{a^2} \sum_{n=1}^{\infty} \exp\left(-D_f \alpha_n^2 t\right) \frac{J_0(r\alpha_n)}{J_1^2(a\alpha_n)} \int r f(r) J_0(r\alpha_n)\, dr \quad (4)$$

where $J_0(x)$ and $J_1(x)$ are the zero and first order Bessel functions of the first kind, and the α_n's are the positive roots of $J_0(a\alpha_n) = 0$. The function $f(r)$ is the initial concentration distribution: $f(r < R_0) = 0.28$ and $f(R_0 < r < a) = 1$. Equation 4 is solved numerically using PYTHON with D_f as the only adjustable parameter.

The model described by equation 4 can predict the evolution of the water concentration as a function of time. In order to compare with the kinetics of front propagation shown in figure 8b, we track the position of the two volume fractions that correspond to the respective phase transitions: $\phi_s = 1 - \phi_w = 0.3$ for the hexagonal-to-micellar interface (blue points) and $\phi_s = 1 - \phi_w = 0.62$ for the cubic-to-hexagonal interface (red points). The model prediction with a diffusion coefficient $D_f = 2.5\,10^{-10}\,\mathrm{mm^2/s}$ is shown with a solid black line in figure 8b. With just one adjustable parameter, it can describe the observed data remarkably well. It captures the different kinetic behavior of the two fronts and even predicts the slight swelling of the drop at the initial stages after contact with water. Note that this diffusion coefficient is approximately two times smaller than the one that best describes the linear penetration results. In the same figure we also show the model prediction for $D_f = 4.55\,10^{-10}\,\mathrm{mm^2/s}$ which of course shows a faster dissolution and movement of fronts. This discrepancy can be attributed to the effect of swelling on the water penetration kinetics. As mentioned above, swelling which without doubt takes place when water is drawn inside the lamellar phase is not explicitly taken into account by this simple model. However, as it is a diffusive-type process its effect on the kinetics is incorporated in D_f. But swelling depends on geometry and the optical images clearly show that it is much more pronounced in the dissolution of cylindrical drops than in linear penetration experiments. As greater swelling generally means lower diffusion coefficients, it can qualitatively explain the difference in D_f between the 2D drops and the 1D linear penetration scans.

Another possibility would be the effect of lamellar phase alignment in the dissolution process. The linear penetration experiments start from a well defined macroscopic alignment of the bilayers perpendicular to the interface (figure 3), whereas on the surface of the cylindrical drop the lamellar phase seems to be randomly aligned. Hence, diffusion of water into the highly aligned lamellar phase should be faster than diffusion into a randomly oriented lamellar phase which wold translate into a higher diffusion coefficient. However, additional experiments (not shown) indicate that the effect of alignment on water penetration kinetics is comparatively very small, so it cannot explain the discrepancy in D_f.

4 Conclusions

We have studied the dissolution of anionic SLE_3S surfactant mesophases in water, using polarized light optical microscopy, in both linear microchannel and circular geometries. Linear solvent penetration experiments of an initially well aligned lamellar (L_α) phase show the formation of a series of planar bands with sharp interfaces whose optical textures allow them to be identified with the cubic, hexagonal, and micellar phases present in the dilution

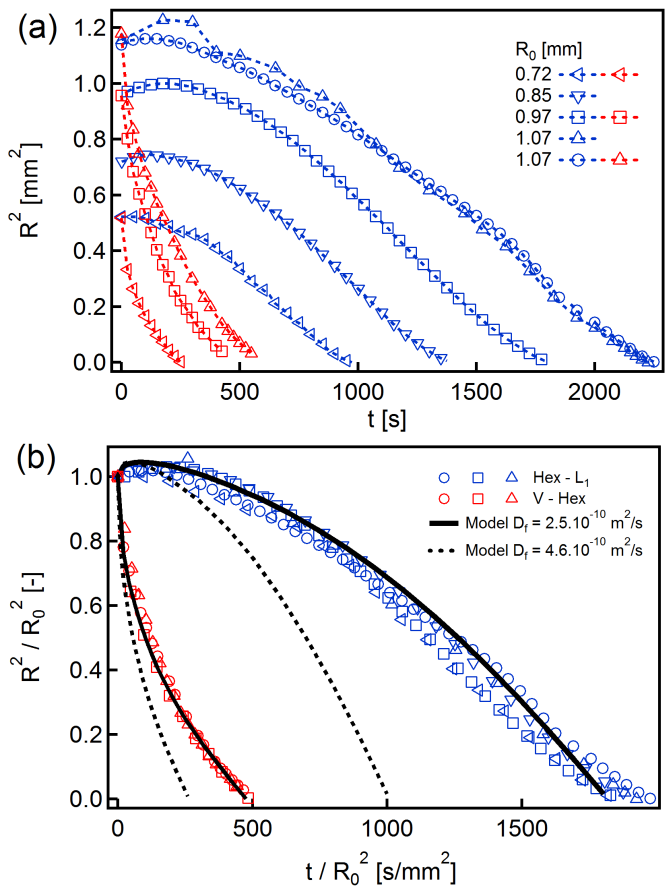

Fig. 8 (a) Kinetics of dissolution of cylindrical surfactant drops. Blue points: radius squared of the dissolving drop (dissolution front) as a function of time for five drops with different initial radii R_0. Red points: radius squared of the cubic to hexagonal interface for three selected drops. (b) Same data plotted with both axes renormalized by R_0^2. Two master curves are obtained for the dissolution front and the cubic to hexagonal front respectively. The solid and dashed lines are predictions of the diffusion model discussed in the text with diffusion coefficients D_f=2.5 10^{-10} mm^2 /s and D_f=4.6 10^{-10} mm^2 /s, respectively.

pathway of the SLE_3S surfactant. It is well known that phase transformation kinetics are fast compared to the timescales of such penetration experiments[11,13]. Hence, each interface tracks a fixed surfactant concentration (ϕ_s) that corresponds to the phase boundaries in the equilibrium phase diagram of the surfactant. By simultaneously tracking the movement of the three interfaces – lamellar-to-cubic ($\phi_s = 0.67$), cubic-to-hexagonal ($\phi_s = 0.62$), and finally hexagonal-to-micellar ($\phi_s = 0.30$) – we show that solvent penetration and dissolution is a diffusive process, and we extract effective diffusion coefficients for each front.

Cylindrical surfactant drop penetration experiments show qualitatively the same succession of cubic, hexagonal, and micellar phases. We experimentally confirm that, as expected, in circular geometry the kinetics of front movement are scaled by the square of the initial drop radius R_0^2.

We further propose a simple model that can explain the time evolution of the surfactant concentration profiles and the diffusive movement of the fronts. This model is based on the idea that the observed behavior stems only from water penetration which locally reduces the surfactant concentration and drives the phase transformations. Remarkably, a single fitting parameter – an effective water diffusion coefficient $D_f = 4.6\,10^{-10}$ mm^2/s can adequately describe the observed movement of all fronts.

This simple model can also accurately describe the kinetics of front movement and dissolution of cylindrical drops, albeit requiring a lower effective water diffusion coefficient $D_f = 2.5\,10^{-10}$ mm^2/s. This is rationalizes in terms of the observed swelling of the surfactant mesophases that is more prominent in cylindrical drops. Swelling tends to slow down front movement and is not explicitly taken into account by the model, and is instead subsumed under D_f.

We also demonstrate the effect of the initial surfactant concentration (ϕ_s^{init}) on the kinetics of dissolution in linear penetration scans. We show that rather counterintuitively the dissolution kinetics are identical when the initial surfactant volume fraction is reduced from 0.72 to 0.5 and only appreciably speed up when ϕ_s^{init} approaches the hexagonal-to-micellar phase boundary at 0.30. The highly non-linear variation is explained by combining our model with the idea that the driving force for water penetration is essentially the difference in osmotic pressure between the neat water and the aqueous environment inside the mesophase that has a high Na^+ surfactant counterion concentration. Our experimental approach and minimal model provide thus a powerful and robust means to investigate dissolution of surfactant mixtures over a wide range of concentrations and estimate dissolution kinetics in geometries.

5 Acknowledgments

We thank Procter & Gamble for financial support and the Engineering and Physical Sciences Research Council (EPSRC) for a knowledge transfer secondment for A.S.P. We thank Brandon M. Vogel (Bucknell University) for discussions on the modelling of diffusion. Data are available on request: please contact polymer-microfluidics@imperial.ac.uk.

References

1 T. Hargreaves, *Chemical formulation: an overview of surfactant based chemical preparations used in everyday life*, Royal Society of Chemistry, Cambridge, 2003.

2 R. G. Laughlin, *The Aqueous Phase Behavior of Surfactants*, Academic Press London, 1994, vol. 6.

3 H. Hoffmann, *Structure and Flow in Surfactant Solutions*, American Chemical Society, 1994, vol. 578, pp. 2–31.

4 H. Li, L. Dang, S. Yang, J. Li and H. Wei, *Colloids and Surfaces A: Physicochemical and Engineering Aspects*, 2016, **495**, 221–228.

5 G. Tiddy, *Physics Reports*, 1980, **57**, 1–46.

6 M. Kahlweit and R. Strey, *Angewandte Chemie International Edition in English*, 1985, **24**, 654–668.

7 M. Gradzielski, *Current Opinion in Colloid & Interface Science*, 2003, **8**, 337–345.

8 B. H. Chen, C. A. Miller, J. M. Walsh, P. B. Warren, J. N. Rud-

dock, P. R. Garrett, F. Argoul and C. Leger, *Langmuir*, 2000, **16**, 5276–5283.
9 P. B. Warren and M. Buchanan, *Current Opinion in Colloid & Interface Science*, 2001, **6**, 287–293.
10 R. G. Laughlin and R. L. Munyon, *The Journal of Physical Chemistry*, 1987, **91**, 3299–3305.
11 P. B. Warren, P. Prinsen and M. A. J. Michels, *Philosophical Transactions of the Royal Society of London Series a-Mathematical Physical and Engineering Sciences*, 2003, **361**, 665–674.
12 H. C. Gerritsen and M. Caffrey, *Journal of Physical Chemistry*, 1990, **94**, 944–948.
13 P. Prinsen, P. Warren and M. Michels, *Physical Review Letters*, 2002, **89**, year.
14 T. L. Rodgers, O. Mihailova and F. R. Siperstein, *J Phys Chem B*, 2011, **115**, 10218–27.
15 M. Buchanan, S. U. Egelhaaf and M. E. Cates, *Langmuir*, 2000, **16**, 3718–3726.
16 L. Reissig, D. J. Fairhurst, J. Leng, M. E. Cates, A. R. Mount and S. U. Egelhaaf, *Langmuir*, 2010, **26**, 15192–15199.
17 M. Caffrey, *Biophysical Journal*, 1989, **55**, 47–52.
18 R. G. Laughlin, *Advances in Colloid and Interface Science*, 1992, **41**, 57–79.
19 R. G. Laughlin, M. L. Lynch, C. Marcott, R. L. Munyon, A. M. Marrer and K. A. Kochvar, *Journal of Physical Chemistry B*, 2000, **104**, 7354–7362.
20 F. Ricoul, M. Dubois, T. Zemb, M.-P. Heck, A. Vandais, D. Plusquellec, I. Rico-Lattes and O. Diat, *The Journal of Physical Chemistry B*, 1998, **102**, 2769–2775.
21 M. U. Araos and G. G. Warr, *The Journal of Physical Chemistry B*, 2005, **109**, 14275–14277.
22 C. Fong, A. Weerawardena, S. M. Sagnella, X. Mulet, L. Waddington, I. Krodkiewska and C. J. Drummond, *Soft Matter*, 2010, **6**, 4727.
23 S. J. Bryant, R. Atkin and G. G. Warr, *Soft Matter*, 2016, **12**, 1645–1648.
24 M. Clerc, P. Laggner, A.-M. Levelut and G. Rapp, *Journal de Physique II*, 1995, **5**, 901–917.
25 J. Leng, M. Joanicot and A. Ajdari, *Langmuir*, 2007, **23**, 2315–2317.
26 L. Daubersies, J. Leng and J.-B. Salmon, *Soft Matter*, 2012, **8**, 5923.
27 L. Daubersies, J. Leng and J.-B. Salmon, *Lab on a Chip*, 2013, **13**, 910.
28 R. G. Rice and D. D. Do, *Chemical Engineering Science*, 2006, **61**, 775–778.
29 P. Costa and J. M. Sousa Lobo, *European Journal of Pharmaceutical Sciences*, 2001, **13**, 123–133.
30 B. A. Miller-Chou and J. L. Koenig, *Progress in Polymer Science*, 2003, **28**, 1223–1270.
31 J. Siepmann and N. Peppas, *Advanced Drug Delivery Reviews*, 2001, **48**, 139–157.
32 P. S. Epstein and M. S. Plesset, *The Journal of Chemical Physics*, 1950, **18**, 1505.
33 D. Readey and A. Copper, *Chemical Engineering Science*, 1966, **21**, 917–922.
34 M. Cable and J. R. Frade, *Journal of Materials Science*, 1987, **22**, 1894–1900.
35 I. Devotta, V. Ambeskar, A. Mandhare and R. Mashelkar, *Chemical Engineering Science*, 1994, **49**, 645–654.
36 J. T. Cabral, S. D. Hudson, C. Harrison and J. F. Douglas, *Langmuir*, 2004, **20**, 10020–10029.
37 C. G. Lopez, T. Watanabe, A. Martel, L. Porcar and J. T. Cabral, *Scientific Reports*, 2015, **5**, 7727.
38 H. P. Martin, N. J. Brooks, J. M. Seddon, P. F. Luckham, N. J. Terrill, A. J. Kowalski and J. T. Cabral, *Soft Matter*, 2016, **12**, 1750–1758.
39 A. S. Poulos, M. Nania, P. Lapham, R. M. Miller, A. J. Smith, H. Tantawy, J. Caragay, J. Gummel, O. Ces, E. S. J. Robles and J. T. Cabral, *Langmuir*, 2016, **32**, 5852–5861.
40 I. Dierking, *Textures of Liquid Crystals*, John Wiley & Sons, 2006.
41 D. C. McDermott, J. McCarney, R. K. Thomas and A. R. Rennie, *Journal of Colloid and Interface Science*, 1994, **162**, 304–310.
42 K. Kocevar and I. Musevic, *Physical Review E*, 2002, **65**, 021703.
43 J. Crank, *The mathematics of diffusion*, Clarendon Press, Oxford, [Eng], 2nd edn, 1975.
44 D. J. Fairhurst, M. E. Baker, N. Shaw and S. U. Egelhaaf, *Applied Physics Letters*, 2008, **92**, 3.
45 M. Dubois, T. Zemb, L. Belloni, A. Delville, P. Levitz and R. Setton, *The Journal of Chemical Physics*, 1992, **96**, 2278–2286.